SAND2011-0763C

Fully micro-fabricated VECSEL at 850nm

Darwin K. Serkland*, Kent M. Geib, Gordon A. Keeler, Gregory M. Peake
Sandia National Laboratories, Albuquerque, NM 87185

ABSTRACT

We report the demonstration of a fully micro-fabricated vertical-external-cavity surface-emitting laser (VECSEL) operating at wavelengths near 850 nm. The external-cavity length is on the order of 25 microns, and the external mirror is a dielectric distributed Bragg reflector with a radius of curvature of 130 microns that is micro-fabricated on top of the active semiconductor portion of the device. The additional cavity length, relative to a VCSEL, enables higher output power and narrower laser linewidth, and micro-fabrication of the external mirror preserves the manufacturing cost advantages of parallel lithographic alignment.

Keywords: VCSEL, vertical-cavity surface-emitting laser, VECSEL, linewidth, spectroscopy, cesium

1. INTRODUCTION

Single-mode 100-MHz-linewidth vertical-cavity surface-emitting lasers (VCSELs) have recently enabled small low-power atomic sensors, including atomic clocks, magnetometers, and gyroscopes, that rely on spectroscopic interrogation of alkali atoms, typically rubidium or cesium, contained in a gas vapor cell.[1-4] A future generation of higher-performance low-power atomic systems is expected to require substantially narrower VCSEL linewidths (in the range of 1 to 10 MHz) in order to be compatible with the natural atomic linewidth (5 MHz for cesium) that is realized with atomic beams, trapped atoms, and trapped ions. Laser output power above 5 mW in a single mode is also needed for many of these higher-performance atomic sensor applications.

Although DFB and DBR lasers can meet the linewidth and single-mode output power requirements, the typical threshold current exceeds 10mA, which is too high for many battery-powered applications. Alternatively, a conventional optically-pumped vertical-external-cavity surface-emitting laser (OP-VECSEL), as shown in Figure 1, can also meet the linewidth and output power requirements[5], but again it consumes more current than most battery-power applications will tolerate. We report here a micro-fabricated VECSEL (micro-VECSEL) with a threshold current of approximately 2 mA, and the potential for increased single-mode output power and narrower linewidth relative to a typical VCSEL. The external cavity length of the micro-VECSEL is less than 1mm, and the external curved mirror is defined by photolithography on the active semiconductor substrate, yielding a transverse alignment accuracy of approximately 1 μm relative to the optical gain aperture.

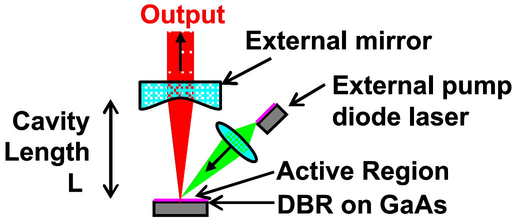

Figure 1. Schematic cross-sectional view of a conventional optically-pumped VECSEL, with cavity length L greater than 5mm.

---

[*] DKSERKL@sandia.gov; phone: (505) 844-5355; fax: (505) 844-8985; http://www.sandia.gov/

2. MICRO-VECSEL FABRICATION

In this section we will discuss the design and fabrication of the micro-VECSEL device, shown schematically in Figure 2.

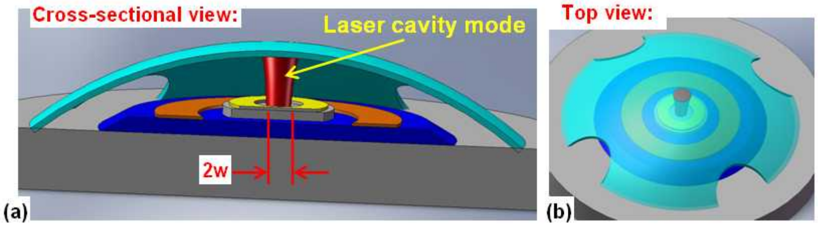

Figure 2. Schematic (a) cross-section and (b) top views of the micro-VECSEL device. The external cavity length shown is 25μm and the radius of curvature of the external mirror is 130μm.

2.1 Micro-VECSEL design

The process that we employed to micro-fabricate the external curved mirror (to be discussed later) yields a relatively short external cavity length of approximately 25 μm. For a plano-concave cavity length fixed at 25 μm, Figure 3(a) shows the calculated mode radius (at the $1/e^2$ intensity point) at the flat (semiconductor) mirror surface.[6] For example, for an external mirror having a radius of curvature of 130 μm, the calculated optical mode diameter at the semiconductor active layers is 7.6 μm. A micro-VECSEL mode diameter of 7.6 μm is approximately twice that of a typical single-mode oxide-aperture VCSEL, suggesting that such a micro-VECSEL could extract four times the single-mode output power of a VCSEL. The cost of the increase in output power will be an increase in threshold current, which will increase with the area of the semiconductor current aperture.

Additionally, the effective cavity length is increased approximately 10-fold, as shown by the 1-D field profile simulation in Figure 3(b). A 10-fold increase in effective cavity length relative to a VCSEL will decrease the cold-cavity linewidth 10-fold and will decrease the lasing linewidth 100-fold.[7-8] Thus, we can expect to reduce the linewidth from 100 MHz for a narrow-linewidth VCSEL to approximately 1 MHz for a narrow-linewidth micro-VECSEL.

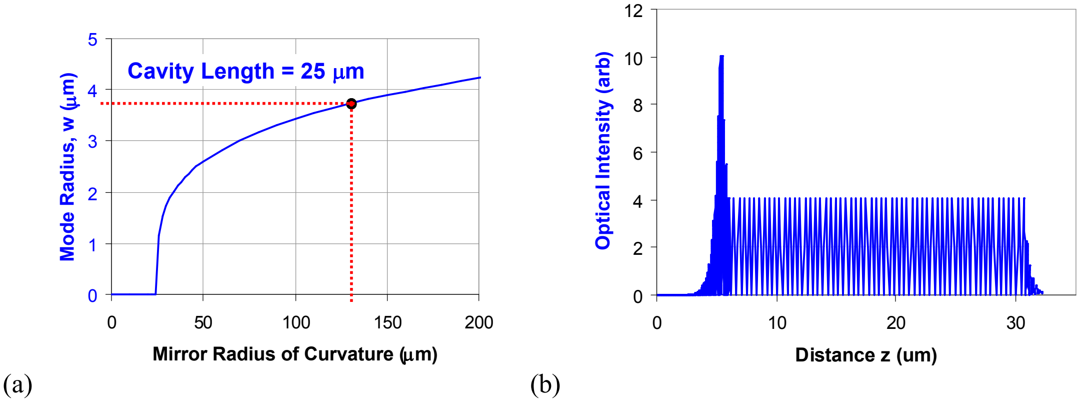

Figure 3. (a) Optical mode radius, w, versus mirror radius of curvature, for a fixed cavity length of 25 μm. (b) Simulated optical field profile versus distance z along the axis of the laser beam.

2.2 Micro-VECSEL semiconductor base structure

A schematic cross-sectional view of the fabricated semiconductor micro-VECSEL base structure is shown in Figure 4(a). The active region contains 5 GaAs quantum wells of thickness 8 nm, positioned at a maximum of the standing wave optical field. The bottom distributed Bragg reflector (DBR) consists of 39 pairs of quarter-wave 16% and 92% AlGaAs layers, yielding a reflectivity above 99.9%. A partial top DBR consists of 8 pairs of quarter-wave 16% and 92% AlGaAs layers, resonating the optical gain provided by the quantum wells. The top DBR is doped p-type, the bottom DBR is doped n-type, and ohmic contacts are applied to each DBR to permit injection of carriers into the quantum wells to create optical gain near 850 nm. Hydrogen ions are implanted around the perimeter of the top p-type DBR mesa to increase the electrical resistance except within the current aperture of diameter D. For this study a range of implant current aperture diameters were fabricated, from 6 to 12 µm, with the intent of matching the plano-concave optical-cavity mode diameter of approximately 8 µm. Figure 4(b) shows a microscope photograph of the micro-VECSEL base structure, with resonant LED emission coming from within the implant aperture diameter D = 12 µm at a bias current of 3 mA.

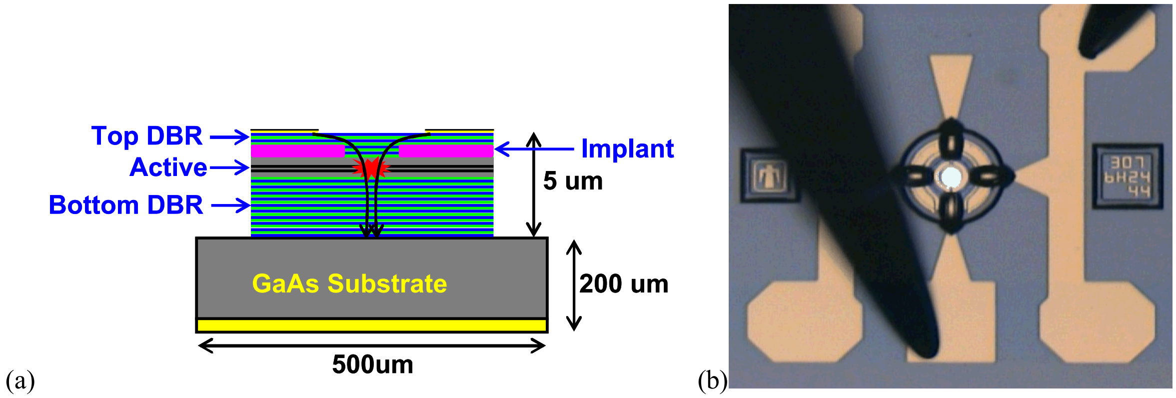

Figure 4. (a) Cross-sectional schematic of the fabricated semiconductor micro-VECSEL base structure. (b) Microscope photograph of resonant-cavity LED emission from the active semiconductor micro-VECSEL base, without an external-cavity mirror.

The electrical and optical device characteristics of the active semiconductor micro-VECSEL base structure are shown in Figure 5. The series resistance of the device is higher than intended due to a problem with the ion implant energy and fluence and because of high lateral spreading resistance in the low-mobility p-type top DBR layers.

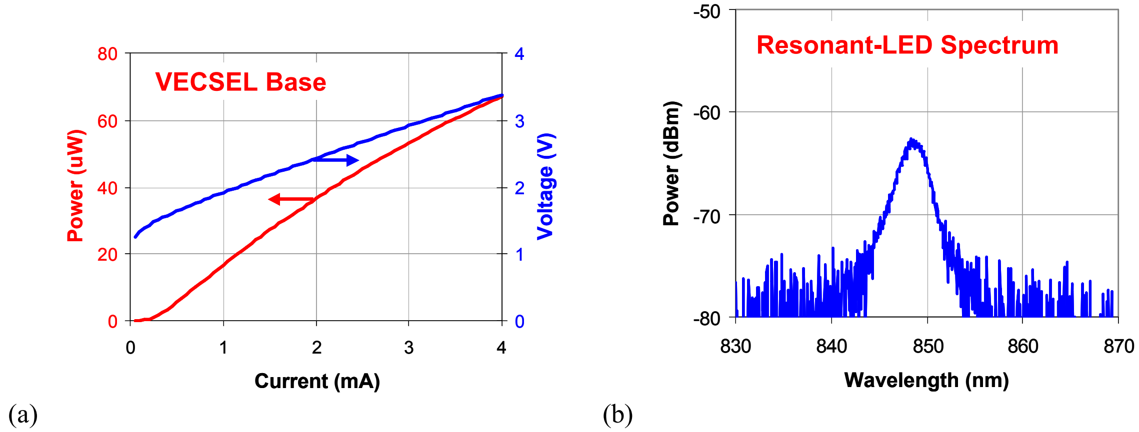

Figure 5. (a) VECSEL base output power and voltage versus injected current, for a device with an implant aperture diameter of 12 µm. (b) Resonant-cavity LED emission spectrum at a drive current of 4 mA into the 12 µm diameter implant aperture.

2.3 Micro-fabricated external curved mirrors

The curved external mirror was fabricated by depositing a dielectric DBR stack onto a spherical photoresist dome. The photoresist dome was fabricated by spinning 20-µm-thick photoresist and patterning circles (cylinders) concentric with the implant apertures using a standard photolithography process. The concentric alignment accuracy of the photoresist cylinders relative to the implant apertures is determined by the photomask alignment. Using our contact mask aligners, relative alignment accuracy on the order of 1 µm is achieved, but better accuracy could be obtained by using a “stepper” mask aligner. Given that the calculated optical mode diameter is about 8 µm, an alignment accuracy of 1 µm should be adequate to yield maximal overlap between the fundamental Gaussian optical mode and the implant gain aperture.

The profile of two patterned photoresist cylinders of diameter 160 and 120 µm is shown in Figure 6(a). The patterned photoresist height measured 20 µm before being reflowed. We reflowed the photoresist by heating it to 200 °C in 2 minutes, and holding at 200 °C for another 2 minutes before cooling to room temperature. The profile of a reflowed 160-µm-diameter cylinder is shown in Figure 6(b). As expected, the reflowed photoresist surface is spherical, as demonstrated by the close agreement with the spherical curve fit shown (in red) in Figure 6(b). For this particular photoresist dome, the radius of curvature is measured to be 131 µm, which is the value chosen in our example calculations above. The height of the photoresist dome has also increased from 20 µm before reflow to 28 µm after reflow. We have modeled the photoresist reflow process and obtained excellent agreement with measurements, assuring us that the process is far more reproducible than is necessary for our purposes. We note that the Gaussian optical mode diameter is not particularly sensitive to either the radius of curvature or the dome height for our chosen design point.

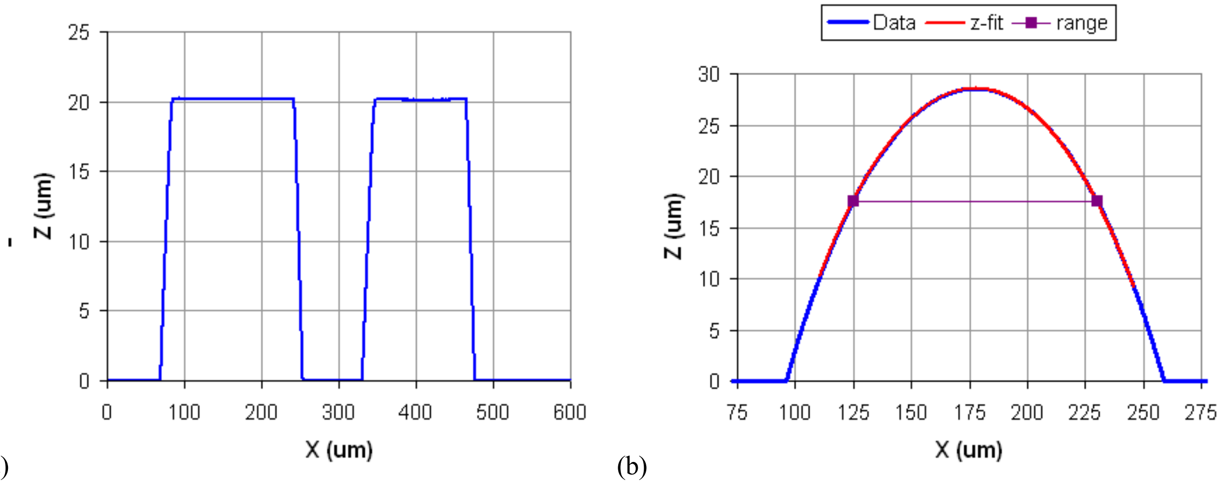

(a) (b)

Figure 6. Photoresist profiles before and after reflow at 200 °C. (a) Profile of 160- and 120-um diameter photoresist cylinders before reflow. The height of the patterned photoresist is 20 um before reflow. (b) Spherical profile of photoresist after reflow of 160-um diameter cylinder.

Plasma-enhanced chemical-vapor deposition (PECVD) was employed to deposit a 6-period dielectric DBR onto the reflowed photoresist domes. The dielectric DBR consisted of 6 pairs of quarter-wave layers of silicon dioxide (SiO2, n=1.46) and silicon nitride (SiN, n=1.96). The measured reflection spectrum of the dielectric DBR, deposited onto a witness silicon wafer, is shown in Figure 7(a). The reflectivity at the center of the stopband was 97% on the silicon wafer, and simulations predict a reflectivity of 90% for the same DBR stack suspended in air (after the photoresist was

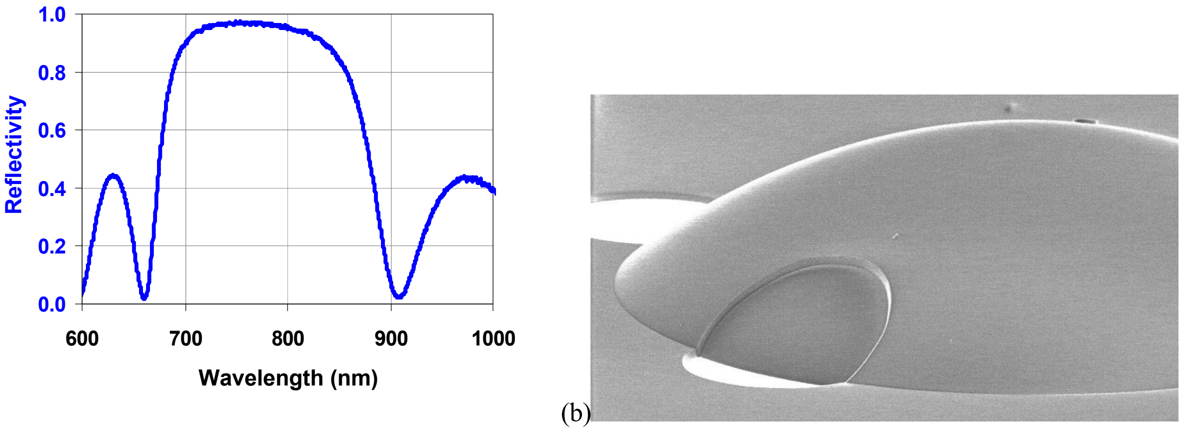

(a) (b)

Figure 7. (a) Reflection spectrum of the 6-period dielectric DBR deposited on a silicon witness wafer. (b) SEM image of photoresist dome covered with a 6-period dielectric DBR. Four holes were dry etched through the dielectric DBR at the perimeter of the photoresist dome, exposing the photoresist.

removed). The center wavelength of the as-deposited dielectric DBR was shorter than the VCSEL design wavelength of 850 nm over most of the sample, which did reduce the yield of our first fabrication run. In order to remove the photoresist from under the curved dielectric DBR, we patterned photoresist over the DBR dome, opening 4 holes at the perimeter of each photoresist dome. The dielectric DBR was etched through those 4 holes, exposing the photoresist at the perimeter of the dome, as shown in Figure 7(b).

The photoresist dome was removed from under the dielectric DBR by ashing in an oxygen plasma at 120 °C for 2 hours. Figure 8(a) shows a microscope image of a dielectric DBR dome that was partially plasma released. The microscope image clearly shows where the photoresist has been removed through two holes in the dielectric DBR at the perimeter of the dome. The other two intended holes, visible in the photograph, did not fully penetrate the DBR, and hence the oxygen plasma could not remove the photoresist from those access points. Figure 8(b) shows a scanning electron microscope (SEM) image of another partially released dielectric DBR dome.

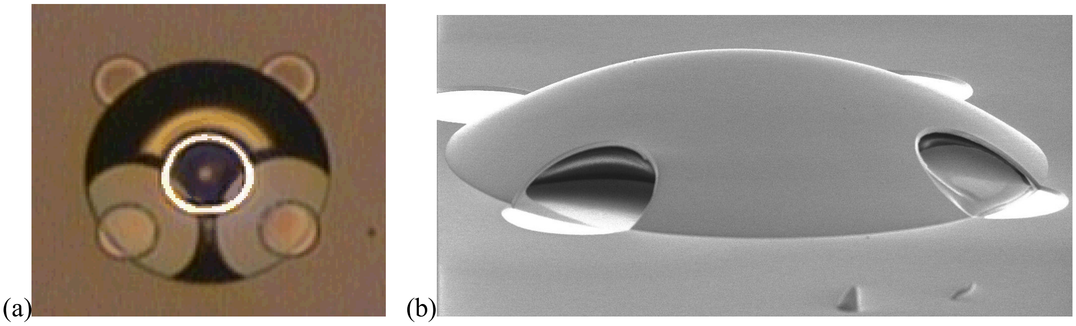

Figure 8. (a) Partially released dielectric DBR, showing that the photoresist has been etched from 2 holes at the perimeter of the photoresist dome. The microscope ring-light illuminator is visible as reflected from the top curved surface (white) and from the flat semiconductor surface (yellow). (b) SEM image of the partially released dielectric DBR.

A fully released dielectric DBR dome, with all of the underlying photoresist removed, is shown in Figure 9(a). A close-up SEM image of the released dielectric DBR dome, at the edge of a release hole, is shown in Figure 9(b). Although the dielectric DBR thickness was only 1.5 µm, and the dome spanned a base diameter of 160 µm, the released dielectric DBR domes appeared to be mechanically robust with no visible damage except where tweezers contacted the wafer or photoresist patterns were defective. We anticipate a fundamental mechanical resonance frequency of the dielectric DBR membrane on the order of 1 MHz, based on comparisons with similar MEMS structures reported in the literature. In the future, we intend to use transparent optical epoxy to under-fill the dielectric DBR domes, in order to improve mechanical robustness of the structure and strongly damp the vibration resonance of the suspended dielectric membrane.

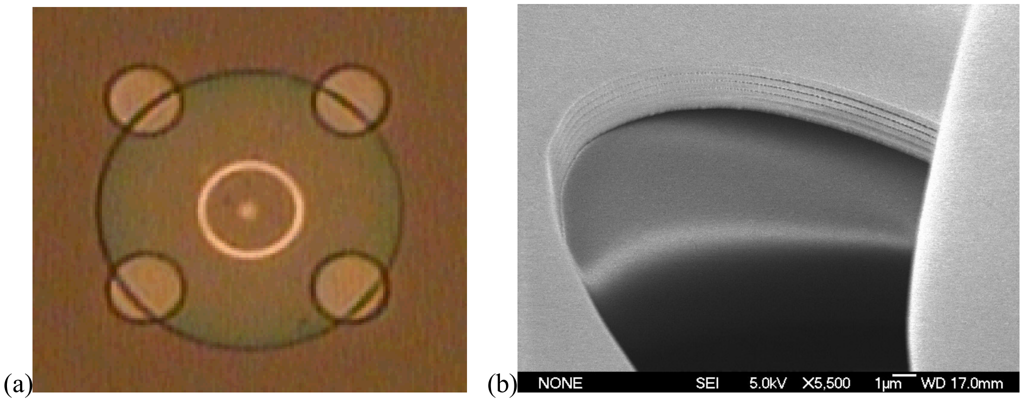

Figure 9. (a) Fully released dielectric DBR dome, after all underlying photoresist was removed using an oxygen plasma. (b) Close-up SEM image of the released dielectric DBR. The 6 periods of the dielectric DBR are clearly visible in this SEM micrograph.

3. MICRO-VECSEL OPERATION DATA

In this section we discuss the measured performance of lasing micro-VECSEL devices.

3.1 Micro-VECSEL LIV data

We fabricated a released dielectric DBR dome over a micro-VECSEL base structure, as described in the previous sections, yielding the micro-VECSEL device shown in Figure 10(a). The photograph shows the micro-VECSEL lasing with an input drive current of 4 mA. The implant aperture diameter for this particular micro-VECSEL was 10 µm. Light power (L) and voltage data (V) versus current for this same device are shown in Figure 10(b). The threshold current was 2.1 mA and the peak output power was 2 mW at a drive current of 6 mA. The series resistance of this device was high (472 Ω), which was due to the implant problem and spreading resistance in the low-mobility p-type material, as discussed previously. Because the as-deposited dielectric DBR wavelength was shorter than the 850-nm VECSEL base wavelength over most of the wafer surface, the yield from this first fabrication run was relatively low. The only lasing devices were found near the rim of the wafer, where the VECSEL base wavelength fell below 850 nm and the dielectric DBR wavelength rose above 800 nm. Nonetheless, it is notable that our very first fabrication run yielded dozens of functioning micro-VECSEL devices, despite many problems in our initial implementation of this new micro-fabrication process flow.

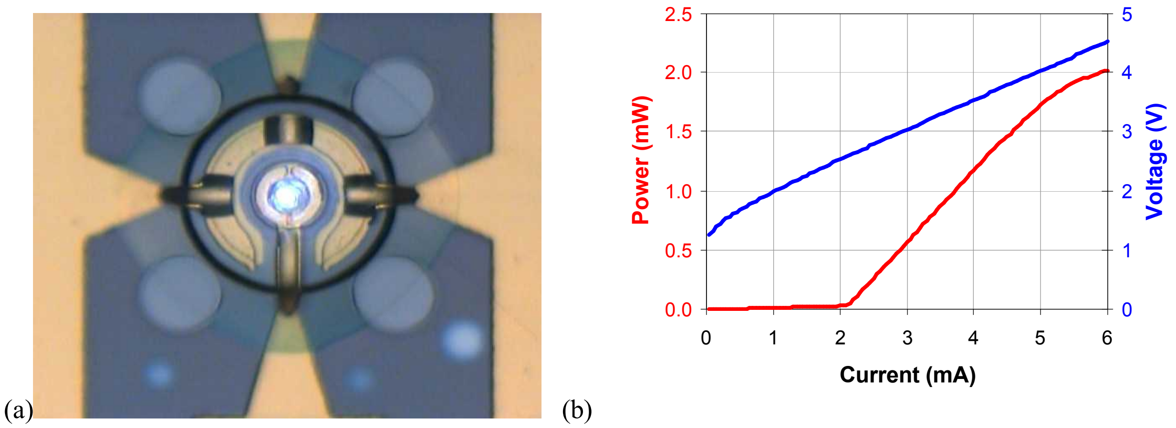

Figure 10. (a) Microscope image of a micro-VECSEL operating with an input current of 4 mA. (b) LIV data of the same micro-VECSEL device, showing a threshold current of 2.1 mA and output power of 2.0 mW at 6 mA input current.

In spite of the several shortcomings of our initial fabrication run, the micro-VECSEL exhibited encouraging performance results. Figure 11 shows the slope efficiency and wall-plug efficiency (WPE) of the same 10-µm-aperture micro-VECSEL discussed above. The slope efficiency was 0.61 W/A, which corresponds to a differential quantum efficiency (DQE) of 41%. The wall-plug efficiency reached a peak value of 8.6% at a drive current of 4.8 mA. Due to

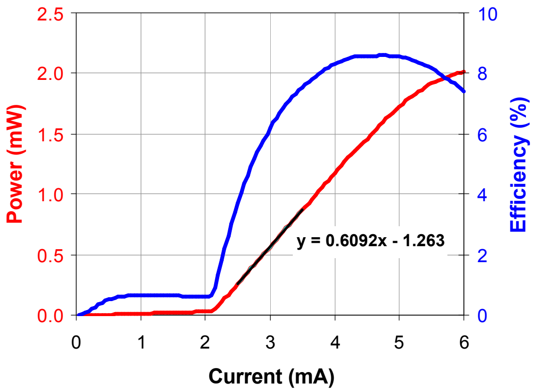

Figure 11. Light power and wall-plug efficiency versus current for the same 10-µm-aperture micro-VECSEL device. A differential quantum efficiency of 41% and a peak wall-plug efficiency of 8.6% were measured from this device.

the shorter-than-intended wavelength of the dielectric DBR, all of the working micro-VECSEL devices on this wafer operated at wavelengths shorter than 850 nm. The data shown in Figure 11 was measured from a micro-VECSEL operating at 842 nm, which was a few nanometers shorter than the peak optical gain wavelength of the GaAs quantum wells. The peak gain wavelength increased rapidly as the device was heated with injection current, causing a large mismatch relative to the cavity resonance wavelength. Thus, we expected the peak output power from this device to be less than ideal.

In addition to the mismatch between the cavity and gain wavelengths, temperature dependent phasing in the external cavity section of the micro-VECSEL limited the output power from the device. Because of the non-zero reflectivity of the top semiconductor DBR employed in this first fabrication run, a coupled cavity existed, and the phase in the external cavity had to be a multiple of π for constructive phasing of the two top reflectors (semiconductor and dielectric DBRs). Only a fraction of the fabricated micro-VECSELs had the proper round-trip phase in the external-cavity section to achieve low threshold current lasing at room temperature. However, due to differences in coefficients of thermal expansions (CTE) of the semiconductor and dielectric materials, and preferential heating of the semiconductor layers when current was injected into the implant aperture, the relative phasing of the two cavities depended on both ambient temperature and the injected current level. The data presented above shows a case of a micro-VECSEL device that was properly phased at room temperature and low injection currents. As the ambient temperature was increased above 25 °C, the threshold current increased due to phase mismatching of the coupled cavities. Similarly, at high injection currents, we believe that phase mismatching also caused the output power to roll over earlier than it otherwise would.

In the future we will attempt two alternative solutions to the coupled-cavity phasing problem. First, the coupled cavity effect can be nearly eliminated by omitting the top semiconductor DBR and anti-reflection coating the top semiconductor facet. In that case, the external DBR reflectivity must be increased to approximately 99.5%, and the external cavity losses should be kept below 0.2%, which seems feasible. The second solution retains the coupled cavity, but adds a thin-film heater that selectively heats the external-cavity section so that the external cavity length can be increased with heat to maintain the proper phase relationship.

3.2 Micro-VECSEL single-mode performance

Finally, we discuss the single-mode performance of the micro-VECSEL devices described above. Polarization-resolved power versus current data is shown in Figure 12(a), which clearly shows that the device operated in a single polarization mode up to thermal roll over. Although nothing was intentionally done to select a single polarization mode, the single polarization performance seemed relatively robust compared to that of typical VCSELs. In the future, it will be interesting to see if single-polarization operation is maintained in devices where the cavity resonance is more closely matched to the peak gain wavelength.

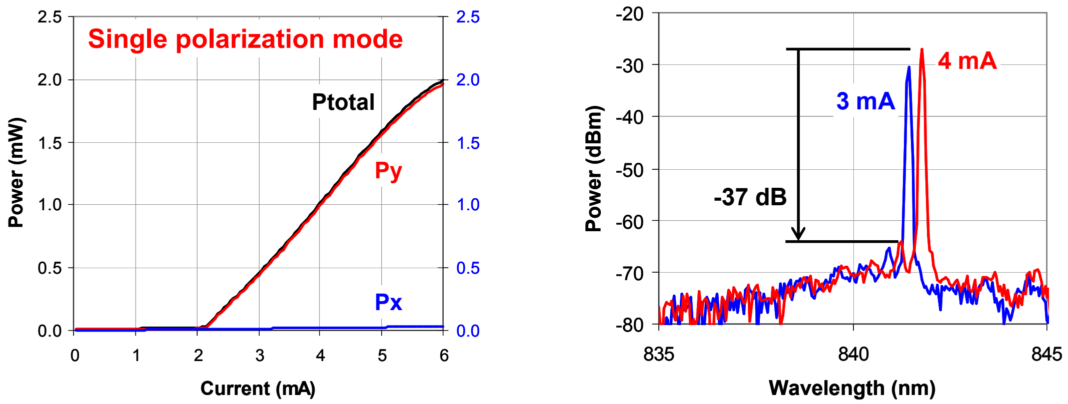

(a) (b)

Figure 12. (a) Polarization-resolved power versus current data, showing a threshold current of 2.1 mA and single-polarization operation to at least 6 mA. (b) Emission spectra at 3 and 4 mA drive current, showing greater than 35 dB side-mode suppression ratio.

Single transverse-mode operation was observed, as shown by the optical emission spectra in Figure 12(b), with side-mode suppression ratios exceeding 35 dB. Operation in a single-transverse mode was anticipated, largely based on the matched spatial overlap of the implant gain aperture and the fundamental Gaussian optical mode of the external cavity. In addition, higher order transverse modes suffered increased optical losses due to diffraction effects of the top metal aperture in the plano-concave cavity.

The short 25-µm external cavity length also yielded a large longitudinal mode spacing (14 nm) relative to the optical gain bandwidth. Thus, much like in a standard VCSEL, single longitudinal mode operation was virtually guaranteed due to the large longitudinal mode spacing. Our measurements of emission spectra from several micro-VECSEL devices confirmed our expectation of operation on only a single longitudinal mode.

4. CONCLUSIONS

In conclusion, we have demonstrated operation of a fully micro-fabricated VECSEL (micro-VECSEL) emitting at wavelengths near 850 nm. We micro-fabricated the external curved mirror on top of the active semiconductor portion of the device by patterning photoresist cylinders concentric with the optical-gain apertures, and reflowing the photoresist to create photoresist domes with spherical surfaces. A dielectric DBR was deposited over the photoresist domes, and the photoresist was removed using an oxygen plasma, yielding curved dielectric mirrors suspended approximately 25 µm above the surface of the active semiconductor layers. We measured a threshold current of 2.1 mA and differential quantum efficiency of 41% from a micro-VECSEL with an implant aperture diameter of 10 µm. The micro-VECSEL operated in a single polarization, transverse, and longitudinal mode up to thermal roll over at an output power of 2 mW.

The additional cavity length of the micro-VECSEL, relative to a VCSEL, enables higher output power and narrower laser linewidth, and micro-fabrication of the external mirror preserves the manufacturing cost advantages of parallel lithographic alignment. In the near future we plan to demonstrate narrow-linewidth micro-VECSELs suitable for use in battery-powered high-performance atomic micro-systems.

ACKNOWLEDGMENTS

The authors wish to thank V. M. Sanchez, V. M. Buscema, T. M. Bauer, and J. B. Clevenger for their expert technical assistance. This work was supported by Sandia, a multiprogram laboratory operated by Sandia Corporation, a Lockheed Martin Company, for the United States Department of Energy's National Nuclear Security Administration under contract DE-AC04-94AL85000.

REFERENCES

[1] J. Kitching, S. Knappe, N. Vukicevic, L. Hollberg, R. Wynands, and W. Weidmann, "A Microwave Frequency Reference Based on VCSEL-Driven Dark Line Resonances in Cs Vapor," IEEE Trans. Instrum. Meas. 49, pp. 1313–1317 (2000).

[2] R. Lutwak, A. Rashed, M. Varghese, G. Tepolt, J. Leblanc, M. Mescher, D. K. Serkland, and G. M. Peake, "The miniature atomic clock - Pre-production results", Proceedings of the 2007 IEEE International Frequency Control Symposium, Geneva, Switzerland, pp. 1327-1333 (2007).

[3] P. D. D. Schwindt, S. Knappe, V. Shah, L. Hollberg, J. Kitching, L.-A. Liew and J. Moreland, "Chip-scale atomic magnetometer," Appl. Phys. Lett. 85, pp. 6409-6411 (2004).

[4] D. K. Serkland, G. M. Peake, K. M. Geib, R. Lutwak, A. Rashed, M. Varghese, G. Tepolt, and M. Prouty, "VCSELs for atomic sensors," Proc. SPIE 6484, pp. 648406-1 to -10 (2007).

[5] M.A. Holm, D. Burns, A.I. Ferguson, M.D. Dawson, "Actively Stabilized Single-Frequency Vertical-External-Cavity AlGaAs Laser," Photon. Technol. Lett., vol. 11, p. 1551 (1999).

[6] A. E. Siegman, *Lasers*, University Science Books, Sausalito, pp. 744-776 (1986).

[7] A. L. Schawlow, and C. H Townes, "Infrared and Optical Masers," Physical Review 112, pp. 1940-1949 (1958).

[8] C. H. Henry, "Theory of the linewidth of semiconductor lasers," IEEE J. Quantum Electronics QE-18, pp. 259-264 (1982).